Additive manufacturing of yttria-stabilized zirconia and lithium silicate electroceramics

By John Zaengle, S.K. Sundaram, and Shawn Allan

Additive manufacturing (AM) has significantly advanced since the late 1990s, with different techniques showing promise for use with advanced materials previously deemed too expensive and difficult to machine.

The energy field is one area in which AM is making inroads. The ability to manufacture precise test pieces quickly with minimal waste can help accelerate the development of advanced material-reliant products like solid oxide fuel cells (SOFCs) and batteries.

Lithography-based ceramic manufacturing (LCM) is particularly interesting for 3D printing of energy materials. Lithography-based AM involves a ceramic powder suspended in a photosensitive resin, with a typical solid loading of 40–50 vol %[1]. Once the part is 3D printed, careful heating allows the binder to be burned out as the remaining structure begins to sinter together. The powder densifies as the part is heated further, forming a final monolithic dense ceramic part.

This investigation summarizes work on two materials of interest for energy generation and storage applications: fully stabilized 8 mol % yttria-stabilized zirconia (YSZ) and lithium silicate powders.

YSZ and lithium silicate for energy applications

A solid oxide fuel cell (SOFC) is a device that converts chemical energy into electrical energy.[2] A SOFC comprises a porous cathode where oxidation occurs and a porous anode where reduction occurs.[3] In between the anode and cathode is a solid electrolyte, which transports oxygen ions from the cathode to the anode. The electrolyte needs to remain chemically and structurally stable at high temperatures and survive the chemical and structural stresses on each side caused by the electrodes.

Yttria-stabilized zirconia (YSZ) has proven a viable electrolyte material in the past because of its abundance, stability, and cost. YSZ has a cubic fluorite structure; the addition of yttria stabilizes the zirconia in the cubic phase. The cubic phase is important for ion conductivity because of dopants like yttria increase intrinsic defects in the structure[4][4]. The defects create vacancies for the oxygen ions as they move through the structure.[6]

The resistance to heating is an important property for SOFCs because electrolyte temperature regulation becomes less critical. Higher conductivity and lower resistance values can be achieved with more stable electrolytes. However, reducing the operating temperature for SOFCs has been a primary focus of recent research to improve usability and broaden potential applications.[7] Nevertheless, electrolytes like 8 mol % YSZ with good thermal and chemical stability are important, leading to the continued interest in YSZ for SOFC.[7] A 3 mol % YSZ powder is commercially available for an LCM system but is only partially-stabilized. Inkjet-based printing is the only AM of 8 mol % or fully stabilized zirconia parts reported in the literature.[1] This study

is an early attempt to AM 8 mol % YSZ using the LCM 3D printing method.

Lithium orthosilicate (Li_4SiO_4) is a lithium-ion conducting electroceramic material. Lithium silicate can be used as an electrolyte for lithium batteries, CO_2 absorption/capture, and solid tritium breeding applications.[8–10] The high lithium atom density and Li^+ interstitials and vacancies have made this material of interest for solid electrolytes in lithium-ion battery development.[8,11]

As energy storage has improved over the past two decades, high capacity and performance batteries are becoming more widespread. Developing a more robust and temperature-resistant battery capable of high cycle rates has become an important target for battery development. The high-lithium content of Li_4SiO_4 ceramics makes it an ideal electrolyte candidate for use at elevated temperatures integrating well with oxide electrode materials.[12] Lithium silicate has a monoclinic structure with lithium vacancies that allow for lithium-ion conduction, which creates the battery's output power; the more vacancies, the better the conduction, and the higher the battery power.[9,12] Cation dopants can be added to the structure; the dopants replace lithium or silicon atoms, allowing more lithium vacancies to form.[13] The addition of dopants improves the conductivity of lithium silicate.

Lithium-containing ceramics have had initial success concerning AM with experimental testing using ink-based printing. Inkjet, direct ink writing, and screen printing have been used to create anode, cathode, andelectrolyte parts for battery applications.[14–16] LCM printing has yet to be applied to lithium silicate powders. This present study is an early attempt at using AM to fabricate lithium silicate using LCM for battery applications.

YSZ and lithium silicate fabrication

Powder and slurries

Five YSZ powders from Inframat Advanced Materials LLC (Manchester, CT) and Tosoh Corporation (Tokyo, Japan) were tested to determine if they could form viable slurries. The ideal powders were 0.5–1 μm in size with a low surface area of ~ 5–7 m^2/g. Two Lithoz binders—MS8 and MS13B—were tested in conjunction with the YSZ powders. The Inframat powders never resulted in a printable slurry. Both Tosoh powders mixed well with MS8 and the MS13B binders. Seven different slurry formulations using Tosoh TZ-8YS or TZ-8Y powders and Lithoz MS13B or MS8 binders were created, as seen in Table I.

Lithium silicate (Li_4SiO_4) powder was synthesized using a solid-state reaction method. Once ground, the powder was sieved through a No. 270 mesh or No. 325 mesh sieve, and two slurries were made using the MS13B binder: Labeled MD-203 (No. 270 mesh, solid loading 48 vol %) and MD-208 (No. 325 mesh, solid loading 51 vol %). MD-203 was not printed because the lithium silicate partially reacted with MS13B binder during storage, causing the slurry to become too viscous to print.

Table I: Tosoh powder-based test slurries.

Lithoz Batch Number	**Powder**	**Binder System**	**Solid loading (Vol %)**
MD-193	Tosoh TZ-8YS	MS13B	42.5
MD-196	Tosoh TZ-8YS	MS8	45.5
MD-171	Tosoh TZ-8YS	MS13B	45.5
MD-143 +202	Tosoh TZ-8YS	MS13B	46.5
MD-195	Tosoh TZ-8YS	MS13B	48.5
MD-192 +194	Tosoh TZ-8Y	MS13B	40
MD-204	Tosoh TZ-8Y	MS8	40

Printing

The MS13B binder printed well when combined with the TZ-8YS powders. Solid loading of 42.5%, 45.5%, 46.5 %, and 48.5% were all tested. Solid loading of 45.5 vol % and 46.5 vol % were the ideal mixtures. MS8 binder combined with TZ-8YS powders did not print as well as the slurries containing MS13B. Tosoh TZ-8YS test slurry had a solid loading of 45.5 vol %. The slurry was used for two prints; the first went relatively well, with the slurry becoming more viscous toward the end of the print (120 layers). The second print reused the residual slurry in the vat of the printer. The second print made it to layer 63 before the slurry was unusable, and the whole print was aborted.

The lithium silicate powders used to make slurry MD-208 had larger than standard particles for printable slurry, resulting in a relatively abrasive or rough slurry. Light penetration was quite high, leading to light scattering, which caused some partial curing around the parts' edges, evident as clumps. The larger particles also caused nonuniform flow properties in the slurry. The larger particle size and solid loading of 51% resulted in the printed parts being relatively weak compared to similar YSZ parts.

Sintering

The printed parts were cleaned of residual slurry, dried, and moved into a drying furnace at 120°C for three days.The drying furnace was preconditioning the parts and fully curing the binder system. After the parts were preconditioned, some small cracks appeared on the surface of larger, thicker parts.

The sintering schedules were adjusted slightly from the first profile seen in Table II, with the second having longer dwell times at lower temperatures. A temperature of 420°C was used for

the binder burnout. Longer dwell times resulted in less cracking and flacking in parts, especially for nonideal slurries like the 42.5 and 48.5 vol % slurries and the TZ-8YS and MS8-based slurry.

Table II: YSZ sintering profiles for short and long dwell times.

Temperature (°C)	**Ramp (°C/min)**	**Short Dwell (h)**	**Temperature (°C)**	**Ramp (°C/min)**	**Long Dwell (h)**
140	0.1	4	135	0.1	16
170	0.2	4	170	0.2	4
250	0.2	2	225	0.2	6
420	0.3	0.01	325	0.3	4
500	1.2	0.01	420	1.2	4
600	1.7	0.01	600	1.5	1
1250	1.7	0.01	1050	1.5	1
1450	3.3	2	1450	2.5	2

Once fired, the parts with thin walls like the turbine found to the right in Figure 4 had no surface damage like cracks or flaking. The turbine was 18 mm in diameter and 10.5 mm tall. Parts with wide layers like the piece to the left in Figure 4, which had printed dimensions 17.5 mm wide and 3 mm tall, resulted in many layers flaking and cracking apart. The Tosoh TZ-8YS samples had cracks between some printed layers, which did not densify together during sintering. This was seen in the 42.5 vol %, 45.5 vol %, and 46.5 vol % solid loading slurries. The 48.5% solid loading slurry only resulted in samples that were printed flat to the build plate. Most parts sintered well. Figure 4 shows two common failures flaking and cracking, and an example of the complex geometry that was successfully sintered.

Figure 4: Tosoh TZ-8YS sintered parts.

After printing, lithium silicate parts had no visible cracking or flaking; however, there were some pinholes on larger samples. During cleaning, the samples had partially cured residue on the edges of the parts. The binder's weak bonding allowed the sharp edges of samples to becomerounded over during a cleaning. Overall, the parts stayed intact with no significant flaws, difficulty removing from the build plate, or difficulties cleaning. Figure 5 shows examples of cleaned samples before being placed in an oven for preconditioning. Parts were preconditioned well; no surface cracks were visible once complete.

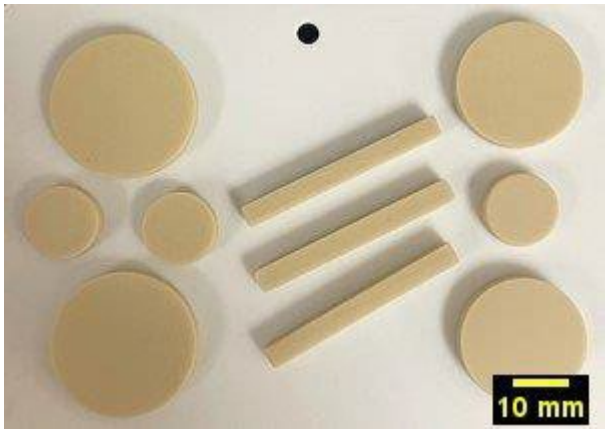

Figure 5: MD-208 lithium silicate parts cleaned before preconditioning.

As shown in Table III, five different sintering profiles were tested, ranging from seven to eight steps. Sintering temperature and dwell times were varied over a narrow range to improve density in the final parts. The fourth and fifth profiles included a step between binder burnout and sintering to heat any unreacted precursors in the material.

Table III: Lithium silicate sintering profiles (* Not Included in Profile).

Temperature (°C)	**Ramp (°C/min)**	**Dwell (h) Profile 1**	**Dwell (h) Profile 2**	**Dwell (h) Profile 3**	**Dwell (h) Profile 4**	**Dwell (h) Profile 5**
130	0.1	3	3	3	3	3
170	0.1	3	3	3	3	3
220	0.1	4	4	4	4	4
250	0.2	5	5	5	5	5

325	0.2	5	5	5	5	5
430	0.5	2	5	5	5	5
680	1	*	*	*	*	5
700	1	*	*	*	5	*
800	1	*	*	5	*	5
900	1	4	5	*	5	*
120	Naturally Cooled	Naturally Cooled	Naturally Cooled	Naturally Cooled	Naturally Cooled	Naturally Cooled

Once sintered, samples printed with the layers perpendicular to the disk's large face had noticeably less bubbling on the samples' surface. The larger surface area between layers led to more bubbling on the surface, as shown in Figure 5, which was sintered at 900°C. Bubbling can be seen on the large round disk with no noticeable bubbling on either smaller disk's surface. The parts were printed, so the layers were perpendicular or parallel to the disk face. All the samples had signs of bubbling on the surface; however, the samples with the smaller surface area layers had noticeably less, with only the side facing up during sintering developing surface bubbles.

The samples in Figure 6 were sintered at a lower temperature of 800°C. The samples sintered using profiles 4 and 5 had noticeably more surface bubbles than the first three profiles tested. The difference being the fourth and fifth profiles had an additional segment added in. The segment held at temperatures in the SSR range was used to make the base powder. The profiles then ramped to a final sintering temperature. The additional step was to provide more time for the samples at an elevated temperature to react, causing CO_2 off-gassing from the leftover precursors used in SSR. The CO_2 was believed to cause bubbling, primarily affecting the sample's top-facing surface. The samples shown in Figure 6 with the small foot were the two densest parts at ~ 90% of actual density.

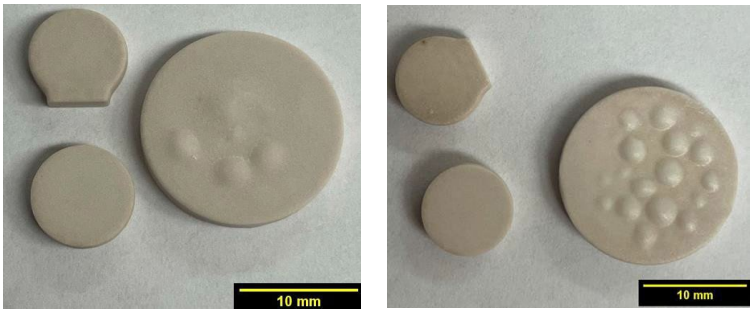

Figure 5: Sintered lithium silicate from sintering profile four top (left) and bottom views (right).

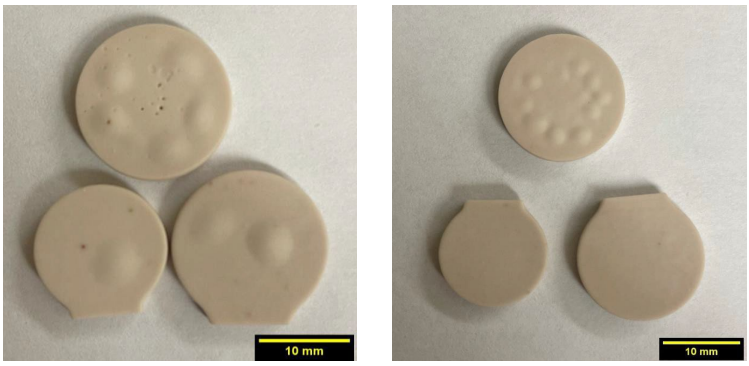

Figure 6: Sintered lithium silicate from sintering profile five top (left) and bottom views (right).

Grain size and density

The two different particle sizes of the Tosoh powders produced samples with different grain sizes, as shown in Table IV. The larger TZ-8YS powders resulted in smaller average grains at 2.7 µm. The TZ-8Y powders had larger graingrowth with an average of 5.3 µm.

Table IV: Tosoh YSZ sintered grain size.

Slurry Solid Loading	42.5*	45.5*	45.5 MS8	46.5*	48.5*	40*	40 MS8
Average Grain Diameter	2.5 µm	3.7 µm	2.6 µm	2.5 µm	2.4 µ m	6.0 µm	4.5 µm
Grain Size Standard Deviation	2.5+/- µm	2.3+/- µm	2.4+/- µm	2.8 +/- µm	2.8+/- µm	5+/- µm	4.5+/- µm
Average Bulk Density	97.9%	95.3%	96.0%	98.3%	97.2%	92.5%	93.4%

* Made with Lithoz MS13B binder.

The sintered TZ-8Y parts had several minor features on the surface compared to the TZ-8YS parts. An example of the feature variation is the presence of small humps on the visible grains' surface. The TZ-8YS grains had prominent features compared to the features seen on the surface of the TZ-8Y samples. The surface variation between the TZ-8YS and TZ-8Y parts shows some correlation between solid loading and particlesizes of the base powder. The TZ-8Y samples had larger grains with a slightly lower density of 93% vs. 97% for the TZ-8YS samples. Figure 7 is an example of the layering from the 3D printing process that remains on the surfaceof

the YSZ parts even after sintering. Figure 7 also includes a close-up of a microcrack in the ceramic structure (left). Figure 8 shows examples of the YSZ surface microstructure. Both have small pores throughout the microstructure.

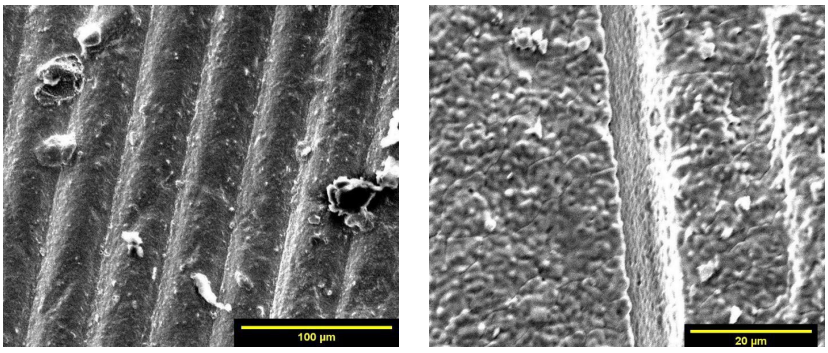

Figure 7: Layered microstructure of sintered YSZ parts.

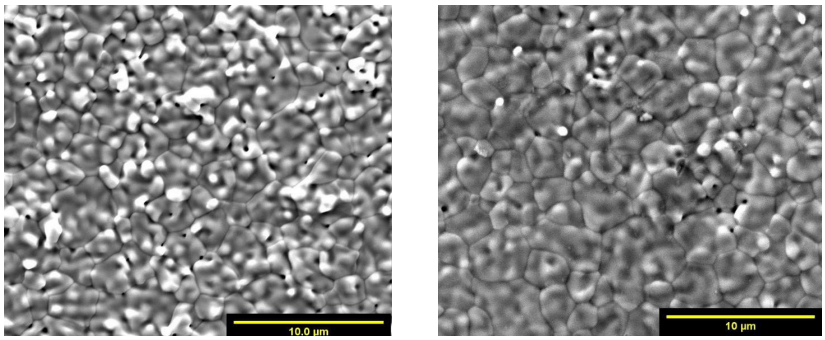

Figure 8: Flat surface microstructure of sintered YSZ parts.

The sintering profiles of the lithium slurries were adjusted to improve bulk density and average grain size. Table V shows how the sintering profiles affected density and grain size. The dwell time for debinding, sintering temperature, and dwell, and later a reaction temperature and dwell were altered to improve density and grain size. Profile 5 had the best results for density with an average of 87%, and the highest parts density was 90%. The samples with a lower surface area between layers relative to size resulted in the best density. Samples that went to higher sintering temperatures of 900°C resulted in larger grain sizes, as seen in profiles 1, 2, and 4, where 3 and 5 sintered at 800°C. Profiles 4 and 5 with an additional step at 680 or 700°C showed improved density and grain size.

Table V: Lithium silicate density and grain size.

	Profile 1	**Profile 2**	**Profile 3**	**Profile 4**	**Profile 5**
Average Density	84%	78%	84%	85%	87%

Average Grain Size (GS)	35 µm	27 µm	18 µm	42 µm	22 µm
GS Standard Deviation	15+/- µm	11+/- µm	9+/- µm	20+/- µm	8+/- µm

When the first three profiles were tested, the sintering temperature and debinding dwell alterations had minimal effect. Profile 4 and 5 included a reaction step to react any carbonates remaining in the material. The result improved density and grain growth. The left of Figure 9 corresponds to the first three profiles and shows pinholes or an open structure. The right of Figure 9 is an example of the microstructure seen in the last two profiles that have improved grain growth and density.

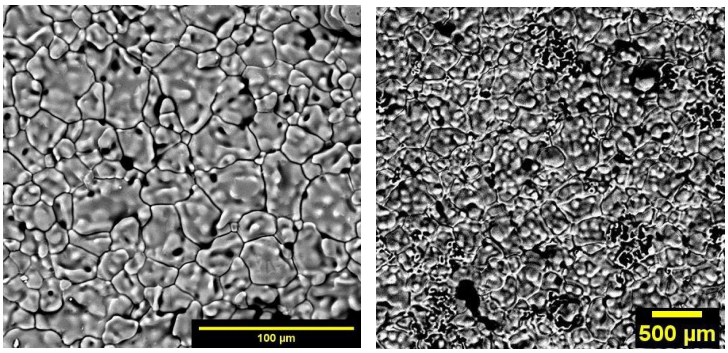

Figure 9: Lithium silicate sintered part using profile three (left) and profile four (right).

Conductivity and activation energy

Impedance spectroscopy was used to determine the activation energy of 3D-printed YSZ and lithium silicate samples. The key features tested were layer orientation to determine if there were any effect on the conductivity and activation energy of the material. AM YSZ samples resulted in a bulk conductivity average of 1.33×10^{-3} Ω-cm at 300°C. AM lithium silicate samples resulted in an average bulk conductivity value of 5.14×10^{-5} S cm^{-1} at 300°C compared to Adnan et al.,[12] who reported a conductivity value of 1.16×0^{-4} S cm^{-1} at 100°C. The conductivity values were less for the AM parts compared to monolithic parts.

Table VI compares the bulk experimental averages found in the literature.[11,26] The bulk activation energy for both lithium silicate layer orientations resulted in 0.22 eV. However, the surface orientation had slightly higher bulk resistance values compared to the layered orientation. The same bulk resistance variation was observed in the YSZ samples, with somewhat higher resistance values for surface orientation samples than layer orientation samples. The bulk activation energy for the two YSZ compositions had a 0.1 eV difference, with the TZ-8Y samples having higher activation energy. Both YSZ and lithium silicate materials demonstrated no significant direct effect on electrical properties caused by varying layer orientation during printing and electrode placement.

Table VI: Bulk activation energy—Experimental vs. literature values.[11,26]

	Experimental Average	Experimental Range Between Samples	Literature Average	Literature Range
Lithium Silicate	0.22 eV	0.01	0.19 eV	0.02
YSZ (TZ-8Y)	0.39 eV	0.01	1.16 eV	0.18
YSZ (TZ-8YS)	0.29 eV	0.01	1.16 eV	0.18

Lithium silicate experimental activation energy was determined for a temperature range of 125–300°C with a printed layer thickness of 100 μm. A 100 μm layer thickness is relatively high compared to typical LCM layers. The experimental average bulk activation energy for lithium silicate was 0.22 eV. The lowest recorded bulk activation energy found was from Adnan et al.,[11,] which was 0.19 eV for samples prepared by sol-gel, pressed into pellets and sintered. The 3D-printed lithium silicate samples had high porosity with an average density of roughly 85% and large outgassing from unreacted precursors, creating large-scale disconnectivity and defects in the materials, thus increasing the activation energy.

YSZ experimental activation energy was determined for a temperature range from 300–500°C with a printed layer thickness of 25 μm. The practical average bulk activation energy was 0.34 eV, with Kwon et al.,[26] reporting bulk activation energies of 1.16 eV. The lower activation energy for the experimental 3D-printed and sintered material may be attributed to electrons potentially finding a path of least resistance not found in traditionally formed parts. The layering may lead to microcracks in the bulk material and uneven sintering, leading to stresses in individual layers, also causing delamination. The thermal profile does not separate debinding from sintering, combining both processes into one. Debinding may be causing tunneling in the microstructure from the escaping binder gases during sintering, leading to a nontraditional microstructure.

Conclusions

Five YSZ powders with two binder systems were tested at varying solids loading percentages. Two powders, the Tosoh TZ-8YS and TZ-8Y and the Lithoz MS13B and MS8 binders, resulted in printable slurries. Seven total variations were successfully printed and sintered. The TZ-8YS powders with a solid loading of 45.5–46.5 % matched with MS13B binder were determined to be the ideal slurry for 8 mol % YSZ. The best-sintered densities achieved for the Tosoh TZ-8YS slurries was 98.3%, and for the Tosoh, TZ-8Y powders were 93.4%.

Five batches of lithium silicate powder were made, resulting in two lithium silicate slurries. The binder used was Lithoz MS13B. The slurry formulations resulted in high curing depths and solid loading amounts. However, the slurry would cure when mixed, so working times were limited to

one week. One lithium silicate slurry was successfully printed and sintered. The slurry contained 51% solid loading and MS13B binder. The best-sintered density for the lithium silicate slurries was 87%.

Samples printed with different layer orientations were tested to determine any significant bulk conductivity variations and activation energy variations using impedance spectroscopy. There was no direct evidence of layer orientation having substantial effects on tested samples' bulk conductivity and activation energies. Preliminary characterization was used to determine how effectively parts could be printed. Micro surface cracking, surface bubbling, and activation energies for conduction revealed a significant difference between traditional manufacturing and AM. These results demonstrate that these materials can be successfully 3D printed and sintered to produce dense products.

Acknowledgments

The authors wish to acknowledge the assistance of The New York State's Division of Science, Technology & Innovation, Empire State Development's FuzeHub Advanced Manufacturing Grant, the Inamori School of Engineering for Teaching Assistant support for J. T. Zaengle. Professor S. K. Sundaram acknowledges the support by Kyocera Corporation in the form of Inamori Professorship. Lithoz America for their assistance in slurry development.

About the authors

John Zaengle is a Ph.D. student and S.K. Sundaram is an Inamori Professor of Materials Science and Engineering at Alfred University. Shawn Allan is vice president of Lithoz America. Contact Zaengle at jtzae16@gmail.com.

References

[1] V. Esposito, C. Gadea, J. Hjelm, D. Marani, Q. Hu, K. Agersted, S. Ramousse, S.H. Jensen, Fabricationof thin yttria-stabilized-zirconia dense electrolyte layers by inkjet printing for high performing solid oxide fuel cells, J. Power Sources. 273 (2015) 89–95. https://doi.org/https://doi.org/10.1016/j.jpowsour.2014.09.085.

[2] K. Kendall, 1 - Introduction to SOFCs, in: K. Kendall, M. Kendall (Eds.), High-Temperature Solid OxideFuel Cells 21st Century (Second Ed., Academic Press, Boston, 2016: pp. 1–24. https://doi.org/https://doi.org/10.1016/B978-0-12-410453-2.00001-4.

[3] M. Ni, T.S. Zhao, eds., Solid oxide fuel cells : from materials to system modeling, Royal Society ofChemistry, Cambridge, UK, 2013.

[4] J.A. Kilner, J. Druce, T. Ishihara, 4 - Electrolytes, in: K. Kendall, M. Kendall (Eds.), High-TemperatureSolid Oxide Fuel Cells 21st Century (Second Ed., Academic Press, Boston, 2016: pp. 85–132. https://doi.org/https://doi.org/10.1016/B978-0-12-410453-2.00004-X.

[5] K. Kendall, 2 - History, in: K. Kendall, M. Kendall (Eds.), High-Temperature Solid Oxide Fuel Cells 21stCentury (Second Ed., Academic Press, Boston, 2016: pp. 25–50. https://doi.org/https://doi.org/10.1016/B978-0-12-410453-2.00002-6.

[6] C. Laberty-Robert, F. Ansart, C. Deloget, M. Gaudon, A. Rousset, Dense yttria stabilized zirconia:sintering and microstructure, Ceram. Int. 29 (2003) 151–158. https://doi.org/10.1016/S0272- 8842(02)00099-8.

[7] K. Rajeswari, M.B. Suresh, U.S. Hareesh, Y.S. Rao, D. Das, R. Johnson, Studies on ionic conductivity ofstabilized zirconia ceramics (8YSZ) densified through conventional and non-conventional sintering methodologies, Ceram. Int. 37 (2011) 3557–3564. https://doi.org/10.1016/j.ceramint.2011.05.151.

[8] A. Choudhary, B.S. Sahu, R. Mazumder, S. Bhattacharyya, P. Chaudhuri, Synthesis and sintering of Li4SiO4 powder from rice husk ash by solution combustion method and its comparison with solid statemethod, J. Alloys Compd. 590 (2014) 440–445. https://doi.org/https://doi.org/10.1016/j.jallcom.2013.12.084.

[9] X. Wu, Z. Wen, X. Xu, X. Wang, J. Lin, Synthesis and characterization of Li_4SiO_4 nano-powders by awater-based sol–gel process, J. Nucl. Mater. 392 (2009) 471–475. https://doi.org/https://doi.org/10.1016/j.jnucmat.2009.04.010.

[10] M.T. Izquierdo, A. Turan, S. García, M. Maroto-Valer, Optimization of Li_4SiO_4 synthesis conditions bysolid state method for maximum CO2 capture at high temperature, J. Mater. Chem. A. 6 (2018) 3249–3257. https://doi.org/10.1039/C7TA08738A.

[11] S.B.R.S. Adnan, N.S. Mohamed, Citrate sol–gel synthesised Li_4SiO_4: conductivity and dielectric behavior, Mater. Res. Innov. 16 (2012) 281–285. https://doi.org/10.1179/1433075X12Y.0000000012.

[12] C.C. Chang, C.C. Wang, P.N. Kumta, Chemical synthesis and characterization of lithium orthosilicate (Li4SiO4), Mater. Des. 22 (2001) 617–623. https://doi.org/https://doi.org/10.1016/S0261-3069(01)00024-3.

[13] C. Masquelier, M. Tabuchi, T. Takeuchi, W. Soizumi, H. Kageyama, O. Nakamura, Influence of thepreparation process on the cation transport properties of $Li_{4+x}M_xSi_{1-x}O_4$ (M = B, Al) solid electrolytes, Solid State Ionics. 79 (1995) 98–105. https://doi.org/https://doi.org/10.1016/0167-2738(95)00037-7.

[14] C.-C. Huang, P.-C. Su, Y.-C. Liao, Conductive lithium nickel oxide thin film patterns via inkjet printingtechnology, Thin Solid Films. 544 (2013) 348–351. https://doi.org/https://doi.org/10.1016/j.tsf.2013.02.101.

[15] K.-Y. Kang, Y.-G. Lee, D.O. Shin, J.-C. Kim, K.M. Kim, Performance improvements of pouch-type flexiblethin-film lithium-ion batteries by modifying sequential screen-printing process, Electrochim. Acta. 138 (2014) 294–301. https://doi.org/https://doi.org/10.1016/j.electacta.2014.06.105.

[16] C. Liu, F. Xu, X. Cheng, J. Tong, Y. Liu, Z. Chen, C. Lao, J. Ma, Comparative study on the electrochemical performance of LiFePO4 cathodes fabricated by low temperature 3D printing, direct inkwriting and conventional roller coating process, Ceram. Int. 45 (2019) 14188–14197. https://doi.org/https://doi.org/10.1016/j.ceramint.2019.04.124.

[17] H. Xu, W. Cheng, X. Jin, G. Wang, H. Lu, H. Wang, D. Chen, B. Fan, T. Hou, R. Zhang, Effect of theParticle Size of Quartz Powder on the Synthesis and CO2 Absorption Properties of Li4SiO4 at High Temperature, Ind. Eng. Chem. Res. 52 (2013) 1886–1891. https://doi.org/10.1021/ie301178p.

[18] A. International, Standard Test Methods for Apparent Porosity, Water Absorption, Apparent Specific Gravity, and Bulk Density of Burned Refractory Brick and Shapes by Boiling Water, ASTM C20-00(2015).(2015).

[19] S. Gates-Rector, T. Blanton, The Powder Diffraction File: a quality materials characterization database,Powder Diffr. 34 (2019) 352–360. https://doi.org/10.1017/S0885715619000812.

[20] R. Mücke, N.H. Menzler, H.P. Buchkremer, D. Stöver, Cofiring of Thin Zirconia Films During SOFCManufacturing, J. Am. Ceram. Soc. 92 (2009) S95–S102. https://doi.org/10.1111/j.1551-

2916.2008.02707.x.
[21] Graphical Representation of Impedance Spectroscopy Data, Impedance Spectroscopy. (2012) 23–35.https://doi.org/https://doi.org/10.1002/9781118164075.ch2.
[22] Fundamentals of Electrochemical Impedance Spectroscopy, Impedance Spectroscopy. (2012) 1–21.https://doi.org/https://doi.org/10.1002/9781118164075.ch1.
[23] Equivalent-Circuit Elements and Modeling of the Impedance Phenomenon, Impedance Spectroscopy. (2012)37–47. https://doi.org/https://doi.org/10.1002/9781118164075.ch3.
[24] Impedance Representation of Bulk-Material and Electrode Processes, Impedance Spectroscopy. (2012) 59–96. https://doi.org/https://doi.org/10.1002/9781118164075.ch5.
[25] M.W. Brown, T. L.; H. Eugene LeMay, J.; Bursten, B. E.; Murphy, C. J.; Woodward, P. M.; Stoltzfus, Chemical Kinetics, in: A. Jaworski (Ed.), Chem. Cent. Sci., 13th ed., Pearson, Upper Saddle River, 2015:pp. 596–597.
[26] O.H. Kwon, G.M. Choi, Electrical conductivity of thick film YSZ, Solid State Ionics. 177 (2006) 3057–3062. https://doi.org/https://doi.org/10.1016/j.ssi.2006.07.039.